

AGN feedback can produce metal enrichment on galaxy scales

M. Villar Martín¹, C. López Cobá², S. Cazzoli³, E. Pérez Montero³, A. Cabrera Lavers^{4,5*}

¹Centro de Astrobiología (CAB), CSIC-INTA, Ctra. de Ajalvir, km 4, 28850 Torrejón de Ardoz, Madrid, Spain

²Institute of Astronomy and Astrophysics, Academia Sinica, No. 1, Section 4, Roosevelt Road, Taipei 10617, Taiwan

³Instituto de Astrofísica de Andalucía, CSIC, Apartado de correos 3004, E-18080 Granada, Spain

⁴GRANTECAN, Cuesta de San José s/n, 38712 Breña Baja, La Palma, Spain

⁵Instituto de Astrofísica de Canarias, Vía Láctea s/n, 38200 La Laguna, Tenerife, Spain

e-mail: villarmm@cab.inta-csic.es

ABSTRACT

Context. Giant (>100 kpc) nebulae associated with active galaxies provide rich information about the circumgalactic medium (CGM) around galaxies, its link with the interstellar medium (ISM) of the hosts and the mechanisms involved in their evolution.

Aims. We have studied the giant nebula associated with the Teacup ($z=0.085$) quasar based on VLT MUSE integral field spectroscopy to investigate whether the well known giant (~ 10 kpc) active galactic nucleus (AGN) induced outflow has an impact on the distribution of heavy elements in and outside the host galaxy.

Methods. We have mapped the oxygen and nitrogen gas relative abundances (O/H and N/O) in two spatial dimensions across the giant nebula and within the galaxy by means of comparing emission line ratios with photoionisation model predictions.

Results. The widely studied AGN driven outflow responsible for the ~ 10 kpc ionised bubble is enhancing the gas metal abundance up to ~ 10 kpc from the AGN. O/H is solar or slightly higher in the bubble edges, in comparison with the subsolar abundances across the rest of the nebula median (O/H ~ 0.63 (O/H) $_{\odot}$).

Conclusions. AGN feedback can produce metal enrichment at large extranuclear distances in galaxies (≥ 10 kpc).

Key words. galaxies: evolution – galaxies: active – galaxies: abundances – quasars: individual: Teacup

1. Introduction

The circumgalactic medium (CGM) is the bound gas halo surrounding galaxies outside their interstellar medium (ISM) and inside their virial radius, extending out to a few hundred kpc. The CGM may be the key regulator of the galactic gas supply. Gas flows occurring between the CGM and the interstellar medium (ISM) are thought to shape galaxies and drive their evolution, via feedback, accretion and recycling of gas. Thus, investigating the metallicity, structure and kinematics of the different gas phases will help us to understand how galaxies gain, eject and recycle the gas during their existence (see Tumlinson et al. 2017 for a review).

Because the CGM is very diffuse and therefore almost invisible in emission, its physical properties remain largely unconstrained. Its understanding has come so far mostly from studies based on absorption lines produced by the CGM around galaxies, imprinted on the spectrum of background objects such as quasars and radio galaxies. The CGM of a few non-active nearby galaxies has also been studied in emission (e.g. Hayes et al. 2016), but the procedure is extremely challenging. The presence of a powerful active galactic nucleus (AGN) can render the CGM gas observable in emission around galaxies up to many 10s of kpc, well into the CGM. Giant emission line nebulae (size ≥ 60 kpc and sometimes >100 kpc) associated with quasars

and radio galaxies at different redshifts have been studied since the 80's (e.g. Baum et al. 1988; McCarthy et al. 1990; McCarthy 1993; van Ojik et al. 1996; Villar-Martín et al. 2003; Borisova et al. 2016; Villar-Martín et al. 2018; Fosfati et al. 2021; Balmaverde et al. 2022; Wang et al. 2023). The discovery of giant (≥ 70 kpc) widely spread reservoirs of molecular gas (e.g. Emonts et al. 2016; Falkendal et al. 2021) associated with several high z ($z \gtrsim 2$) radio galaxies reveals a multiphase CGM that was chemically enriched when the Universe was 3 Gyr old and supplies gas from which galaxies grow.

Wide field integral field spectroscopic instruments on 8-10 meter telescopes, such as the Multi Unit Spectroscopic Explorer (MUSE) on the Very Large Telescope (VLT), have opened excellent opportunities to detect and study in great detail the elusive material from the warm ($T < 10^5$ K) ionised CGM around powerful active galaxies at different redshifts thanks to the illumination by the powerful AGN. If it were not for the excitation by the AGN continuum, this gas might not be detected or would only be observable through absorption line studies.

The object of this work is the well known Teacup radio quiet type 2 quasar at $z = 0.085$. It shows a ~ 10 kpc loop of ionised gas resembling a handle of a teacup (hereof its nickname), which was discovered by volunteers of the Galaxy Zoo project (Keel et al. 2012) and has been widely studied in the context of AGN feedback and its potential impact on galaxy evolution. The system has been proposed to be the scenario of a giant outflow generated either by an

* Based on observations made at Paranal Observatory under programme ID 0102.B-0107

AGN wind or induced by a 1 kpc radio jet whose effects are noticed up to at least ~ 10 kpc from the AGN and might be responsible for the bubble-like morphology (Gagne et al. 2014; Harrison et al. 2015; Keel et al. 2015; Ramos Almeida et al. 2017; Villar-Martín et al. 2018; Moiseev & Ikhsanova 2023; Venturi et al. (2023, hereafter V23).

Villar-Martín et al. (2018) discovered a >100 kpc ionised nebula associated with this object (see also Villar Martín et al. 2021, which could be a product of a merger that occurred 1-2 Gyr ago (Keel et al. 2015). This rich gas reservoir, which extends into the CGM, has been rendered visible due to the activity of the quasar nucleus. AGN photoionisation dominates the excitation of the spatially resolved gas emission up to its boundary (Gagne et al. 2014; Villar-Martín et al. 2018; V23; Moiseev & Ikhsanova 2023), except at some locations outside the putative quasar ionisation cones where evidence for shock excitation has been found (V23). Stellar photoionisation could also contribute to ionise the gas locally in some tidal features. The large scale kinematics are strongly reminiscent of rotation (Villar-Martín et al. 2018; Moiseev & Ikhsanova 2023) and tentative results suggest subsolar nebular abundances ($\sim 0.5 Z_{\odot}$, Villar-Martín et al. 2018). The well known bubble appears to be expanding from the nucleus and out into the nebula.

We present in this paper a detailed optical spectroscopic study of the Teacup nebula based on VLT-MUSE archival data with the main goal of mapping the gas abundances in two spatial dimensions. The ultimate science goal is to establish whether the giant outflow has an impact on the distribution of heavy elements from the nucleus on large spatial scales. We will discuss the results in the context of other studies of the CGM and its role in the evolution of galaxies.

The paper is organised as follows: the data and analysis method are presented in Sect. 2 and 3 respectively. The latter includes the description of the methods used to derive the gas chemical abundances and physical properties of the gas. The results are presented in Sect. 4 and discussed in Sect. 5. The main conclusions are summarised in Sect. 6.

Throughout this paper, we assume flat Λ CDM cosmology following Planck Collaboration et al. (2020), with $H_0 = 67.4 \text{ km s}^{-1} \text{ Mpc}^{-1}$, $\Omega_m = 0.31$. This gives a spatial scale of $1.65 \text{ kpc arcsec}^{-1}$ at $z = 0.085$.

2. Data

The data were collected for the 0102.B-0107 program (principal investigator, PI: L. Sartori; see V23 for details) with the European Southern Observatory (ESO) Very Large Telescope (VLT) and the Multi Unit Spectroscopic Explorer (MUSE, Bacon et al. 2010). This instrument covers a $1' \times 1'$ field of view (FoV) in the Wide Field Mode (WFM), with a spatial sampling of $0.2'' \text{ pix}^{-1}$. The wavelength coverage is $\sim 4650\text{-}9300 \text{ \AA}$ with a $1.25 \text{ \AA} \text{ pix}^{-1}$ spectral sampling and a resolving power $R = \lambda/\Delta\lambda \sim 1700\text{-}3400$ ($\Delta V \sim 176\text{-}88 \text{ km s}^{-1}$).

The observations were performed in March 2019. The processed archive data cube was used for this study. The Teacup ionised nebula fills a large fraction of the MUSE FoV. Separate sky cubes are not available from these observations. Sky oversubtraction due to contamination of the sky spectrum by object emission was identified at a few spatial locations of very low surface brightness which appeared as artefacts that mimic absorption features adja-

cent to the strongest emission lines (specially $[\text{OIII}]\lambda 5007$). Because our attempts to improve the sky subtraction did not achieve significant improvements, we finally used the archive cube. To further evaluate the potential impact of this effect, a comparison with the processed archive datacube from program 0103.B-0071 (PI: C. Harrison) was also performed. Although separate sky cubes were obtained for this program, the resulting sky subtraction was not significantly better. The comparison was in any case valuable to characterise the impact of the sky subtraction on the data quality. The artefacts are in general faint in comparison with the emission lines and are shifted in wavelength so that they could be efficiently identified and isolated. We confirm that imperfections on the sky subtraction do not affect our results and conclusions. These are all based on the 0102.B-0107 datacube because of the significantly better seeing (FWHM= $0.74''$ vs. $1.3''$ for the 0103.B-0071 program) and of somewhat better signal-to-noise ratio (SN).

3. Analysis

3.1. Spatially resolved emission line flux measurements

Our main goal is to map the electron temperature, T_e , and the oxygen abundance O/H in two spatial dimensions to investigate whether the giant outflow has an impact on the distribution of heavy elements across the galaxy and out into the CGM. For the T_e determination, it is essential to measure the flux ratio of a nebular to an auroral emission line, such as the $[\text{OIII}]\lambda 5007/\lambda 4363$ (or $[\text{NII}]\lambda 6583/\lambda 5755$). For this, we defined spatial apertures at different locations through the nebula and extracted the integrated spectrum from each one.

The apertures were selected based on the visual inspection of the $[\text{OIII}]\lambda 5007$ morphology at different wavelengths (i.e. velocities) scanned through the line profile. These scans reveal striking morphological changes with velocity and are specially useful to identify some faint structures, such as tidal tails, arcs, knots, filaments, which have similar velocities (Fig. 1). By restricting the central λ and the width, $\Delta\lambda$, of the narrow band images, the contrast of the lowest surface brightness features is enhanced and the spatial apertures covering them can be defined with greater accuracy to maximise the SN of the integrated spectra. This was useful to detect faint emission lines through the largest possible extension, while preserving at the same time the morphological information on the diversity of nebular structural elements.

The map of the positions of the resulting 64 selected apertures is shown in Fig. 2 (left panel). We also show in adjacent panels of the same figure the W_{80} and V_s maps based on $[\text{OIII}]\lambda 5007$. W_{80} is the velocity width that encloses 80% of the total line flux and V_s is the velocity shift relative to the narrow core of the nuclear $[\text{OIII}]$ line, considered here as indicator of the systemic velocity (Greene & Ho 2005). These maps can be directly compared with those of V23, that were based on a spaxel by spaxel analysis. The huge dimensions of the nebula both along and perpendicular to the radio axis are apparent. Although some prominent features stand out (knots, filaments, etc), gas emission seems to fill the entire area within the nebular outer boundaries. The large scale rotation pattern (Gagne et al. 2014; Villar-Martín et al. 2018; Moiseev & Ikhsanova 2023) and

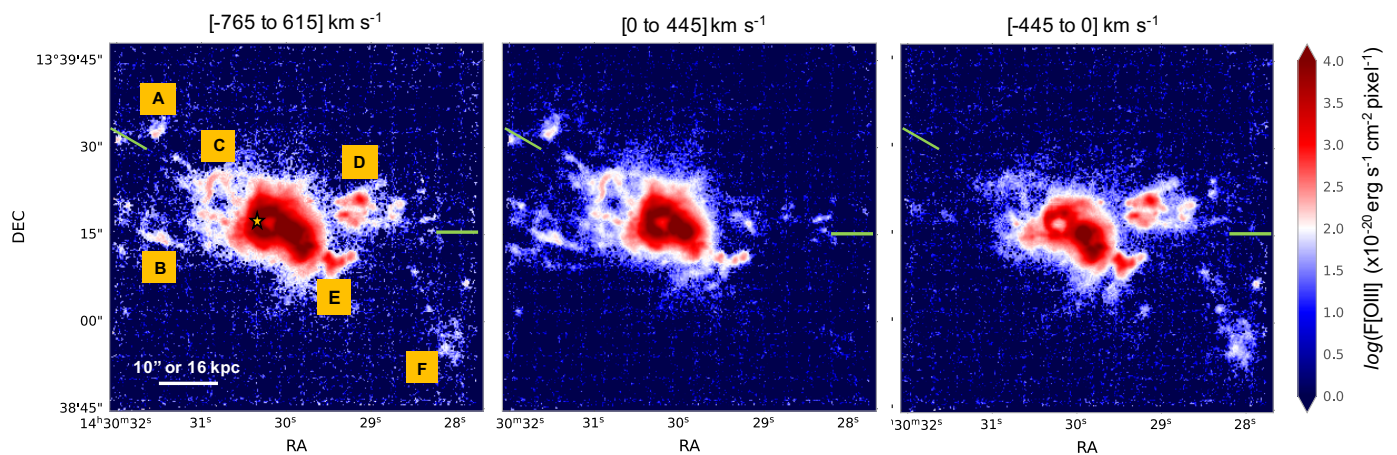


Fig. 1. [OIII] continuum subtracted images covering different spectral windows that were selected to highlight the diversity of nebular morphological features. Each image covers a different velocity (i.e. spectral) range relative to the nuclear systemic velocity as indicated at top. The nebular morphology strongly varies with velocity. The left panel shows the total [OIII] flux narrow band image. The well known ~ 10 kpc ionised bubble is marked with a tiny yellow star in the left panel. The green lines indicate the position angles of the radio axis to the NE and to the W (Harrison et al. 2015). To guide the reader, the letters ‘A’ to ‘F’ mark some emission line features that can also be identified in the mask map of Fig. 2.

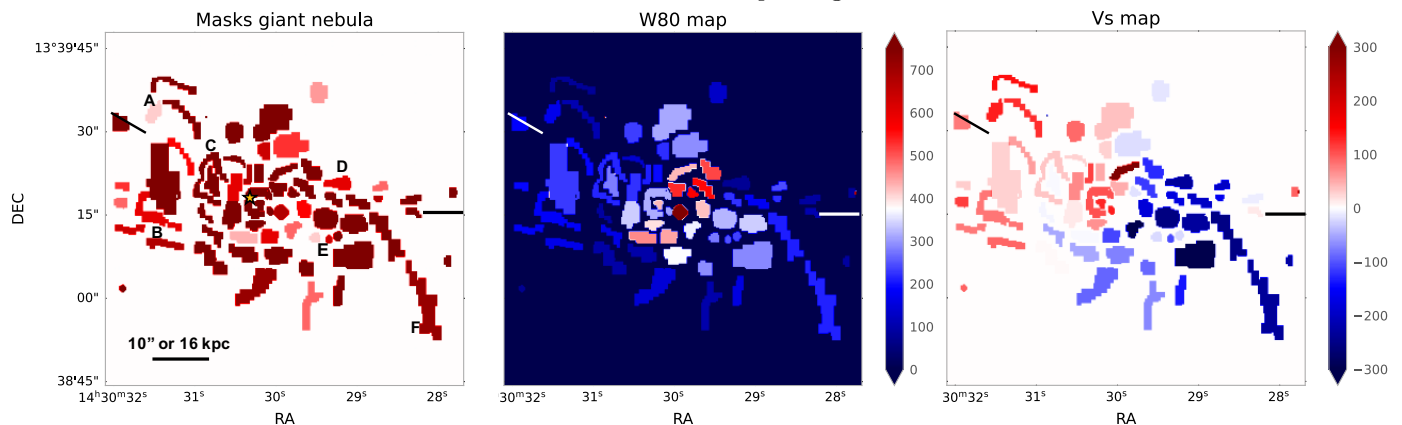


Fig. 2. Map of the masks used in our analysis (left) and [OIII] kinematic maps (middle and right panels). The colours in the first map have no particular meaning but help differentiating the apertures. A 1D spectrum was extracted from each one, so that a single W_{80} and V_s (middle and left panels) values are associated to each aperture. V_s is the velocity shift relative to the narrow core of the nuclear [OIII] line. The maps cover the total MUSE FoV ($\sim 1' \times 1'$). W_{80} and V_s are in km s^{-1} . Letters ‘A’ to ‘F’, yellow star and solid lines have the same meaning as in Fig. 1.

the enhanced width, W_{80} , of the lines in the direction perpendicular to the radio axis are clear (V23).

The 1D spectra extracted from the individual apertures were used to measure the fluxes of the lines involved in our analysis: [OIII] $\lambda\lambda 4959, 5007$ and $\lambda 4363$, H γ , H β , H α , [NII] $\lambda\lambda 6548, 6583$, and $\lambda 5755$ and [SII] $\lambda\lambda 6716, 6731$.

For a subset of spectra the stellar continuum was relatively strong compared with the emission line fluxes, that is, the equivalent width of the lines was low, so that it was first necessary to fit it and subtract it. The effects of stellar absorption can affect the Balmer emission lines and need to be accounted for to obtain accurate reddening estimates. It was also necessary in several spectra to reconstruct the H γ and [OIII] $\lambda 4363$ baseline and recover both line fluxes. The continuum was fitted for each spectrum with the PYPPIPE3D tool (e.g., Lacerda et al. 2022), that performs a decomposition of the observed stellar spectra into multiple simple stellar populations, each of different age and metallicity. As a test, we also subtracted the continuum with the method described in Cazzoli et al. (2022). The results were consistent.

We also checked the reddening inferred from H γ /H β and H α /H β in the final, corrected spectra. Case B H α /H β =2.87 and H γ /H β =0.47 were assumed. Reddening estimations from both ratios are in general consistent within the errors. Changing these values within the range H α /H β =2.76-3.05 and H γ /H β =0.45-0.47 (Osterbrock 1989) has no significant impact. The E_{B-V} values implied by H α /H β were used for extinction correction since they have smaller errors. Using instead the E_{B-V} implied by H γ /H β has also a negligible impact on the results.

3.2. Derivation of temperatures and gas chemical abundances

We used the python code PYNEB (Luridiana et al. 2015) to estimate T_e of [OIII] for spectra with detected [OIII] $\lambda 4363$ using [OIII] $\lambda 5007/\lambda 4363$, and, when possible, of [NII] using [NII] $\lambda 6583/\lambda 5755$. This code was also used to infer the electron density n_e using [SII] $\lambda\lambda 6717, 6731$. We calculated the corresponding errors by applying to the calculations a

Monte Carlo iteration using the nominal fluxes perturbed with the observational errors.

For the derivation of abundances, the direct method (i.e. the derivation of total chemical abundances from their ionic fractions and the measured electron temperature) cannot be satisfactorily applied for the case of the Narrow Line Regions (NLR) in Active Galactic Nuclei (AGN) (e.g. Dors et al. 2015). Instead, we used the code HII-CHI-MISTRY (hereafter HCM, Pérez-Montero 2014). The approach of this code consists of a bayesian-like comparison between certain reddening-corrected ratios of emission line fluxes relative to a recombination H line ($H\beta$ in our case), that are sensitive to total oxygen abundance (O/H), nitrogen-to-oxygen ratio (N/O), and ionisation parameter (U), with the predictions from a large grid of photoionisation models. In particular, we used version 5.3 of HCM, which considers models calculated under the most usual conditions in the NLR of active galaxies. As a result, the most probable values and their uncertainties for O/H, N/O and $\log(U)$ are obtained.

The grid of models is explained in detail in Pérez-Montero et al. (2019). The gas is assumed to be distributed homogeneously with a filling factor of 0.1 and a constant electron density of $n_e=500 \text{ cm}^{-3}$. The densities across the Teacup nebula are however significantly lower ($n_e \lesssim 150 \text{ cm}^{-3}$, see Table .1 and V23). Since collisional de-excitation effects are not relevant for the line ratios under consideration in this density regime, the inferred abundances are not affected by the comparatively high density used in the models (Pérez-Montero et al. 2019).

The Spectral Energy Distribution (SED) was considered to be composed by two components: one representing the Big Blue Bump peaking at 1 Ryd, and the other a power law with spectral index $\alpha_{\text{OX}}=-1.2$ representing the non-thermal X-rays radiation (see Pérez-Montero et al. 2019 for additional details). The stopping criterion to measure the resulting emergent spectrum is that the proportion of free electrons in the ionised gas is lower than 2%. The models consider a Mathis et al. (1977) grain size distribution and a dust-to-gas mass ratio of 7.5×10^{-3} (Rémy-Ruyer et al. 2014).

The grid of models vary the oxygen and nitrogen abundances within $12+\log(\text{O}/\text{H})=6.9-9.1$ in bins of 0.1 dex and $\log(\text{N}/\text{O})=-2.0-0.0$ in bins of 0.125 dex, respectively. The rest of chemical abundances are scaled in the models with respect to oxygen following the solar proportions, $12+\log(\text{O}/\text{H})=8.69 \pm 0.04$, given by (Asplund et al. 2021). In accordance with these authors, we also assumed $12+\log(\text{N}/\text{H})=7.83 \pm 0.07$ for the Sun.

The original grid of models in Pérez-Montero et al. (2019) covers values of $\log(U)$ from -4.0 to -0.5 in bins of 0.25 dex, although we only assumed $\log(U) > -2.5$ to break the degeneracy with U for the ratios of high- to low-excitation lines in the optical range predicted by the models. This restriction does not imply any significant change in the derivation of the chemical abundances (see Pérez-Montero et al. 2019 for a better clarification). The code also provides uncertainties to the derived quantities calculated as the quadratical addition of the standard deviation of the obtained bayesian distribution with the uncertainty obtained from a Monte Carlo iteration through the given input nominal flux of each line perturbed with its corresponding observational error.

4. Results

We show in Table .1 the O/H and N/O abundances predicted by photoionisation models for different apertures, as well as the [OIII] and [NII] electron temperatures inferred with PYNEB for the densities estimated with [SII] $\lambda\lambda 6716, 6731$ (see Sect. 3.2). The observed extinction corrected line ratios relative to $H\beta$ and measured with the 1dim spectra are also shown. This analysis was performed for a set of 23 (including the nucleus) apertures where [OIII] $\lambda 4363$ has been detected (see left panel in Fig. 3). The top (lower) part of the table comprises the apertures in which [NII] $\lambda 5755$ is detected (undetected). This does not affect the estimated chemical abundances, but simply indicates whether $T_{[\text{NII}]}$ could be inferred or not. The O/H, N/O and $T_{[\text{OIII}]}$ information in Table .1 is also shown as 2dim maps in Fig. 3 and 4.

The main result which stands out in Fig. 3 is that the giant ionised bubble shows significantly higher O/H and lower $T_{[\text{OIII}]}$ than the gas at most locations across the giant nebula. This is confirmed in all apertures along the bubble edge, where $12+\log(\text{O}/\text{H})$ is in the range $8.68 \pm 0.09-8.77 \pm 0.12$. As in the nucleus (8.66 ± 0.11), these abundances are consistent with the solar value or slightly higher.

For the rest of the nebula (this is, the extended gas outside and beyond the bubble), except in Ap. 13, the oxygen abundances are subsolar everywhere (as tentatively found by Villar-Martín et al. 2018). Considering all apertures across the nebula, the \log of the median is $12+\log(\text{O}/\text{H})=8.49$ (or 63% solar), with values as low as $8.37 \pm 0.08-8.44 \pm 0.13$ (48%-56% solar) in Ap. 15, 16, 19, 21, 22. Interestingly, the gas encircled by the bubble edges (Ap. 11), with $12+\log(\text{O}/\text{H})=8.53 \pm 0.17$ (69% solar), shows an intermediate abundance between the most enriched gas (the bubble edges) and the more metal poor gas in the rest of the nebula.

It is important to highlight that the abundance predictions are based on the assumption that the gas is photoionised by the AGN everywhere. This is reasonable for most apertures except, possibly, at a few positions located in the direction perpendicular to the main axis of the nebula, where shocks might be contributing to the excitation of the gas (V23). These apertures are labelled Ap. 12, 18, 19 in Fig. 3, left panel. In spite of this uncertainty, the fact that (except for Ap. 13) this gas follows the general behaviour of the O/H and $T_{[\text{OIII}]}$ maps suggests that the derived abundances are reliable.

In general, the $T_{[\text{OIII}]}$ map (right panel in Fig. 3) mimics the behaviour of the O/H maps in an anticorrelation. The nucleus shows the minimum temperature, $T_4=T_{[\text{OIII}]} / 10^4 = 1.27 \pm 0.08 \text{ K}$, in comparison with the rest of the gas, which shows $T_4 > 1.5$ everywhere. As before, the bubble stands out in this map, with the edges being significantly colder ($T_4 \sim 1.5-1.6$ in Ap. 3 to 9) than the giant nebula, which is very hot with $T_4 \sim 1.7-1.9$ almost everywhere. V23 presented a 2dim $T_{[\text{OIII}]}$ map tracing the nucleus and the ionised bubble. They inferred a narrow range of significantly lower $T_{[\text{OIII}]} \sim (1.3-1.4) \times 10^4 \text{ K}$ compared to our estimations. The reason for this discrepancy remains unknown.

In regard to the N/O abundance (Fig. 4 and Table .1), the most obvious result is the much higher nuclear value ($\log(\text{N}/\text{O})=-0.56 \pm 0.08$, i.e. roughly twice the solar abundance ratio of -0.86 ± 0.07), compared with the so-

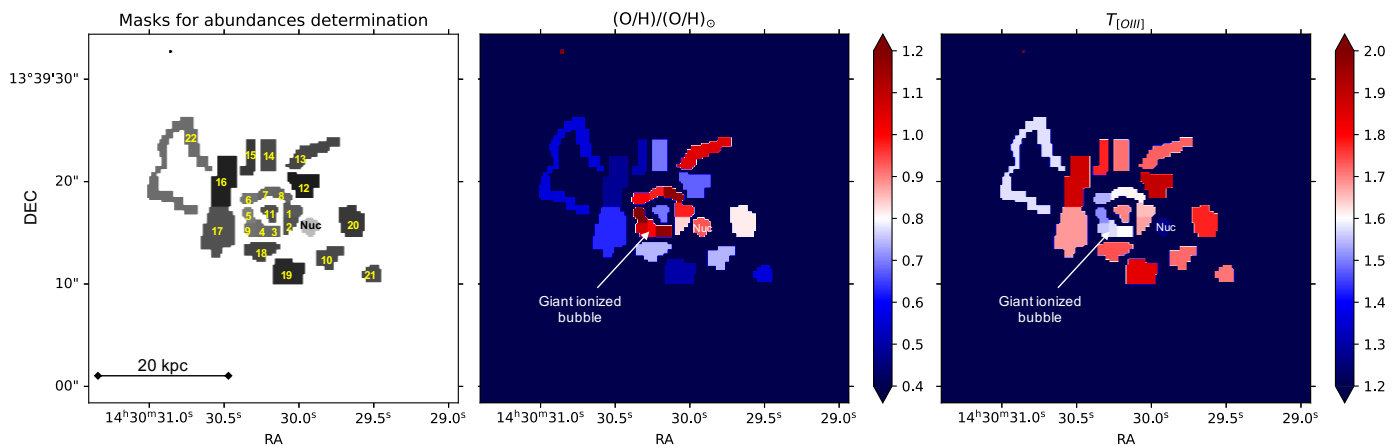


Fig. 3. Maps of $(O/H)/(O/H)_{\odot}$ ratio and $T_{[OIII]}$. The masks used in this analysis are shown in the left panel. They correspond to the apertures for which $[OIII]\lambda 4363$ is detected. Notice that the FoV is smaller than in Fig. 1 and 2. The exact values of O/H and $T_{[OIII]}$ are in Table .1. $T_{[OIII]}$ is in units of 10^4 K.

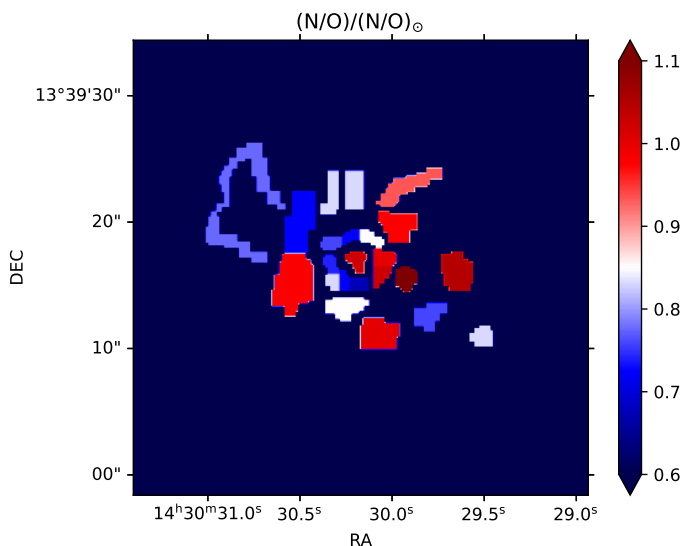


Fig. 4. Map of $(N/O)/(N/O)_{\odot}$. The FoV is the same as in Fig. 3. The nuclear value is 1.99, which is outside the colour bar range to enhance the contrast for visualisation purposes. The $(N/O)/(N/O)_{\odot}$ values are in Table .1.

lar or somewhat below solar N/O everywhere else ($-1.03 \pm 0.09 \leq \log(N/O) \leq -0.84 \pm 0.20$), including the bubble edge. There is not such a striking trend of N/O with location as found for O/H. The bubble edge shows among the lowest N/O ratio ($\sim 68\text{-}85\%$ N/O_{\odot}), although not unique in comparison with other regions of the giant extended nebula. The bubble edge N/O values are lower than the gas encircled by it (ap. 11), the nucleus and the gas in between (ap. 1 and 2).

$T_{[NII]}$ could be measured only for the nucleus and up to the bubble edge (Table .1). The temperature difference between these two regions is less pronounced than for $T_{[OIII]}$. $T_{4[NII]} \sim 0.983 \pm 0.066$ K in the nucleus and somewhat higher in the bubble ($\sim 1.01\text{-}1.12$ K).

5. Discussion

With a maximum extension as traced by the MUSE data of ~ 126 kpc (this is a lower limit since the gas fills the FoV in this direction), the Teacup giant nebula traces part of the CGM. Its properties are strongly conditioned by the AGN, but it still provides valuable information about the CGM. If it was not for the nuclear activity, most (if not all) of this gas would remain invisible.

The giant nebula shows subsolar abundances, with $O/H \sim (48\%\text{-}84\%) \times (O/H)_{\odot}$ almost everywhere, and median 63%, well below the nuclear, roughly solar abundance. For comparison, different works based on absorption line studies have shown that the dense gas in the CGM of $z \lesssim 1$ galaxies has a bimodal metallicity distribution function, with an equal number of absorbers in the low-metallicity ($Z \lesssim 0.03Z_{\odot}$) and high-metallicity ($Z \sim 0.4Z_{\odot}$) branches (e.g. Lehner et al. 2013; Wotta et al. 2016). The abundance of the Teacup ionised nebula falls in the latter group (clearly, this does not discard the presence of lower metallicity gas). The high-metallicity branch has been proposed to trace galactic winds, recycled outflows, and tidally stripped gas (Lehner et al. 2013).

Lower CGM metallicities compared with the ISM have been found for different galaxy types, based on studies of absorption line systems at $\lesssim 200$ kpc from their host galaxies (e.g. Kacprzak et al. 2019). These authors found a large range of abundances in the CGM of isolated star forming galaxies, $0.01 \lesssim Z/Z_{\odot} < 1$ and an offset of $\log(dZ) = -1.17 \pm 0.11$ between the CGM and ISM, which shows no dependence with stellar mass. The relation has a large scatter of $1\sigma = 0.72$. The offset for the Teacup is smaller for O/H ($\log(dZ) \sim -0.17$ using the median nebular O/H), although still within the scatter. Different processes may be at work in this system, related to the nuclear activity and/or to its merger history.

We have shown that the ~ 10 kpc Teacup bubble to the East of the nucleus, that is known to be driven by an AGN wind or the small nuclear radio jet, is associated with obvious changes in the gas abundance. The bubble edge shows significantly higher O/H (solar or slightly solar, similar to the nucleus) in comparison with the subsolar O/H across the rest of the nebula. Most likely as a consequence, the

bubble edge is also significantly less hot ($T_4 \sim 1.5-1.6$) than the rest of the nebula ($1.7 \lesssim T_4 \lesssim 1.9$). Therefore, the outflow appears to be causing a change in the gas metal content from the nucleus up to ~ 10 kpc.

This mechanism may also explain the nuclear deficit of O/H. For the Teacup values of $\log(M_*/M_\odot) = 11.15 \pm 0.05$ and star forming rate $SFR \sim 10 M_\odot \text{ yr}^{-1}$ (Jarvis et al. 2020; Ramos Almeida et al. 2022), $12 + \log(\text{O}/\text{H}) \sim 8.85$ is expected, according to the mass-metallicity-SFR (M_* -Z-SFR) relation by Pérez-Montero et al. (2013) or ~ 8.8 for the extrapolation of the M_* -Z-SFR relation by Andrews & Martini (2013) to high M_* . Seyfert 2 galaxies with similar M_* tend to show O/H consistent with these predictions (Pérez-Díaz et al. 2021). The Teacup nucleus, on the contrary, shows lower than expected O/H (8.66 ± 0.05), while the nuclear N/O (-0.56 ± 0.08 , Table .1) is consistent with that expected for its M_* ($\log(\text{N}/\text{O}) = -0.54$, Pérez-Montero et al. 2013; Andrews & Martini 2013).

The dilution produced by inward flows of low-metallicity gas (for instance, from the outskirts of the two merging galaxies) could explain the nuclear O/H and N/O (Edmunds 1990; Rupke et al. 2010). The outflow is also an interesting possibility. This scenario is supported by the similar O/H of the bubble edge and the nuclear gas, which is moreover enhanced in comparison with the rest of the nebula. On one hand, radiative outflows can couple more efficiently with metals via resonance line scattering (e.g. Pauldrach et al. 1994; Arav et al. 1994; Higginbottom et al. 2024; see also Edmunds 1990). On the other, galaxies show metallicity gradients such that the inner regions have higher abundances (Searle 1971; Kewley et al. 2019; Maiolino & Mannucci 2019). Based on this, a gradient is expected to exist within the ~ 4 kpc diameter nuclear aperture used in the Teacup analysis. The outflow has been generated in the inner regions ($\lesssim 1$ kpc) close to the AGN (Harrison et al. 2015; Ramos Almeida et al. 2017; V23), where the gas is expected to be more metal rich. If it drags gas out to large distances, as proposed in this scenario, the global metallicity of the residual gas within the nuclear aperture would be lower as a consequence.

An implication of this scenario is that the outflow has been capable of ejecting gas from the galaxy center and dragged it up to ~ 10 kpc. If the outflow expanded without displacing significant amounts of gas to large distances, the bubble abundance would be similar to the rest of the nebula. The implications are important. It supports that metal-enriched galactic outflows (driven by an AGN in this particular case) shape the mass-metallicity relationship, by removing metals from galaxy potential wells and ejecting them to large distances, possibly out into the CGM (Tremonti et al. 2004; Peeples et al. 2014; Chisholm et al. 2018; Tortora et al. 2022).

The behaviour of N/O remains to be explained. An outflow could preserve N/O (Edmunds 1990 (specific modeling would be valuable for AGN generated winds)). On the contrary, this ratio is depleted in the bubble edge in comparison with the nucleus and its gradient shows no obvious spatial correlation with the bubble, but just a tentative trend to show among the lowest N/O. This is not necessarily a discrepancy. Given the complexity of the N/O behaviour in terms of secondary and primary stellar production processes, and the fact that the ejected gas would mix with gas across the nebula with a non-uniform N/O distribution, it

is difficult to predict how this ratio would behave as the bubble expands and mixes with the pre-existing reservoir.

An alternative scenario to gas ejection from the centre is that local chemical enrichment has been produced by young stars. This is supported by the detection of blue-coloured continuum emission co-spatial with the bubble edge due to a population of stars that are younger ($\lesssim 100-150$ Myr) than in the rest of the galaxy ($\gtrsim 0.5-1$ Gyr, V23). According to these authors, widespread star formation has been triggered at the edge of the bubble due to the compressing action of the jet and outflow (positive feedback). The time scale could be long enough to enrich the local gas with O, but not with secondary N (Mollá et al. 2006; Kumari et al. 2018). This would explain the enhanced O/H in comparison with the rest of the nebula, while N/O is not clearly different, and being at the same time significantly lower than in the nucleus.

Yet another possible scenario to explain the abundance values in the bubble relates to the depletion by dust of metals from the gas-phase ISM. If shocks destroyed dust as the bubble expands (e.g. Dopita et al. 2018), metals could be released to the gas. Since oxygen is more sensitive to depletion than nitrogen (Jones & Ysard 2019), this could explain the higher O/H of the bubble in comparison with the rest of the nebula, while having a tentatively lower N/O.

Whether due to nuclear gas ejection, to local star formation or dust destruction, in all three scenarios the AGN induced outflow is responsible for the metal enrichment of the gas at distances as large as ~ 10 kpc. The implications are different. In the ejection scenario, the behaviour of O/H provides observational evidence of how AGN induced outflows can deprive the central regions of galaxies from metals and transfer them up to very large distances, possibly out of the galaxy and into the CGM. In the second scenario, the behaviour of O/H provides evidence of how AGN induced outflows can produce local metal enrichment (this is also the case in the third, the dust depletion scenario) at very large distances from the nucleus, with a delay between the quasar onset and the induced metal enrichment of $\sim 100-150$ Myr.

6. Conclusions

The giant ($\gtrsim 126$ kpc) nebula associated with the Teacup QSO2 at $z = 0.085$ traces part of its CGM. Its properties are strongly influenced by the nuclear activity up to the outer detected emission line regions, where it still provides valuable information about the CGM surrounding the quasar host galaxy. If it was not for the nuclear activity, most (if not all) of this gas would remain invisible. This study is an example of the great potential of studying giant nebulae to investigate in emission the CGM around active galaxies at all redshifts.

The widely studied AGN driven outflow responsible for the well known ionised bubble is enhancing the gas metal content (O/H) up to ~ 10 kpc from the AGN. The giant nebula shows subsolar metallicity almost everywhere, except the bubble, which has about solar or slightly super-solar metallicity.

This could be a consequence of the ejection of metal rich gas from the nucleus. In such scenario, the Teacup provides observational evidence for how AGN feedback can deprive the central regions of galaxies from gas and displace metals out to very large distances, possibly out of the galaxy. It

supports that metal-enriched AGN outflows can shape the mass-metallicity relationship of galaxies. Alternatively, the O/H enrichment could have been produced locally by the young stellar population formed in the bubble edge, possibly formed as a consequence of positive feedback ~ 100 -150 Myr (V23). A third possibility is the release of oxygen to the gas phase as a consequence of dust destruction in the bubble by shocks triggered by the expanding outflow.

In any of the scenarios considered, the nuclear activity is the ultimate mechanism responsible for the metal enrichment of the gas at large extranuclear distances (~ 10 kpc).

Acknowledgements. We are grateful to Luc Binette, Bjorn Emonts and Bruno Rodríguez for useful feedback. We also thank the referee for the careful revision of the manuscript and valuable suggestions. MVM and ACL research has been funded by grant Nr. PID2021-124665NB-I00 by the Spanish Ministry of Science and Innovation/State Agency of Research MCIN/AEI/ 10.13039/501100011033 and by "ERDF A way of making Europe". SC acknowledges financial support from the Severo Ochoa grant CEX2021-001131-S and the Ministry of Science, Innovation and Universities (MCIU) under grants PID2019-106027GB-C41. EPM acknowledges financial support by project Estalidos8 PID2022-136598NB-C32 (Spanish Ministry of Science and Innovation). The Cosmology calculator by Wright (2006) has been used.

References

- Andrews, B. H. & Martini, P. 2013, *ApJ*, 765, 140
 Arav, N., Li, Z.-Y., & Begelman, M. C. 1994, *ApJ*, 432, 62
 Asplund, M., Amarsi, A. M., & Grevesse, N. 2021, *A&A*, 653, A141
 Bacon, R., Accardo, M., Adjali, L., et al. 2010, *Proc. SPIE*, 7735, 773508
 Balmaverde, B., Capetti, A., Baldi, R. D., et al. 2022, *A&A*, 662, A23
 Baum, S. A., Heckman, T. M., Bridle, A., et al. 1988, *ApJS*, 68, 643
 Borisova, E., Cantalupo, S., Lilly, S. J., et al. 2016, *ApJ*, 831, 39
 Cazzoli, S., Hermosa Muñoz, L., Márquez, I., et al. 2022, *A&A*, 664, A135
 Chisholm, J., Tremonti, C., & Leitherer, C. 2018, *MNRAS*, 481, 1690
 Dopita, M. A., Vogt, F. P. A., Sutherland, R. S., et al. 2018, *ApJS*, 237, 10
 Dors, O. L., Cardaci, M. V., Hägele, G. F., et al. 2015, *MNRAS*, 453, 4102
 Edmunds, M. G. 1990, *MNRAS*, 246, 678
 Emonts, B. H. C., Lehnert, M. D., Villar-Martín, M., et al. 2016, *Science*, 354, 1128
 Falkendal, T., Lehnert, M. D., Vernet, J., et al. 2021, *A&A*, 645, A120
 Fossati, M., Fumagalli, M., Lofthouse, E. K., et al. 2021, *MNRAS*, 503, 3044
 Gagne, J. P., Crenshaw, D. M., Kraemer, S. B., et al. 2014, *ApJ*, 792, 72
 Greene, J. E. & Ho, L. C. 2005, *ApJ*, 627, 721
 Harrison C. M., Thomson A.P., Alexander D. M., Bauer F.E., Edge A.C., Hogan M.T., Mullaney J. R., Swinbank A. M., 2015, *ApJ*, 800, 45
 Hayes, M., Melinder, J., Östlin, G., et al. 2016, *ApJ*, 828, 49
 Higginbottom, N., Scepi, N., Knigge, C., et al. 2024, *MNRAS*, 527, 9236
 Jarvis, M. E., Harrison, C. M., Mainieri, V., et al. 2020, *MNRAS*, 498, 1560
 Jones, A. P. & Ysard, N. 2019, *A&A*, 627, A38.
 Kacprzak, G. G., Pointon, S. K., Nielsen, N. M., et al. 2019, *ApJ*, 886, 91
 Keel, W. C., Chojnowski, S. D., Bennert, V. N., et al. 2012, *MNRAS*, 420, 878
 Keel, W. C., Maksym, W. P., Bennert, V. N., et al. 2015, *AJ*, 149, 155
 Kewley, L. J., Nicholls, D. C., & Sutherland, R. S. 2019, *ARA&A*, 57, 511
 Kumari, N., James, B. L., Irwin, M. J., et al. 2018, *MNRAS*, 476, 3793
 Lacerda, E. A. D., Sánchez, S. F., Mejía-Narváez, A., et al. 2022, *New A*, 97, 101895
 Lehner, N., Howk, J. C., Tripp, T. M., et al. 2013, *ApJ*, 770, 138
 Luridiana, V., Morisset, C., & Shaw, R. A. 2015, *A&A*, 573, A42
 Maiolino, R. & Mannucci, F. 2019, *A&A Rev.*, 27, 3
 Mathis, J. S., Rumpl, W., & Nordsieck, K. H. 1977, *ApJ*, 217, 425
 McCarthy, P. J., Spinrad, H., van Breugel, W., et al. 1990, *ApJ*, 365, 487
 McCarthy, P. J. 1993, *ARA&A*, 31, 639
 Mannucci, F., Cresci, G., Maiolino, R., et al. 2010, *MNRAS*, 408, 2115
 Martin, D. C., Matuszewski, M., Morrissey, P., et al. 2015, *Nature*, 524, 192
 Martin, D. C., O'Sullivan, D., Matuszewski, M., et al. 2019, *Nature Astronomy*, 3, 822
 Mollá, M., Vílchez, J. M., Gavilán, M., et al. 2006, *MNRAS*, 372, 1069
 Moiseev, A. V. & Ikhsanova, A. I. 2023, *Universe*, 9, 66
 Osterbrock, D. E. 1989, *Astrophysics of Gaseous Nebulae and Active Galactic Nuclei*, by Donald E. Osterbrock. Published by University Science Books, ISBN 0-935702-22-9
 Pauldrach, A. W. A., Kudritzki, R. P., Puls, J., et al. 1994, *A&A*, 283, 525
 Peebles, M. S., Werk, J. K., Tumlinson, J., et al. 2014, *ApJ*, 786, 54
 Pérez-Díaz, B., Masegosa, J., Márquez, I., et al. 2021, *MNRAS*, 505, 4289
 Pérez-Montero, E., Contini, T., Lamareille, F., et al. 2013, *A&A*, 549, A25
 Pérez-Montero, E. 2014, *MNRAS*, 441, 2663
 Pérez-Montero, E., Dors, O. L., Vílchez, J. M., et al. 2019, *MNRAS*, 489, 2652
 Planck Collaboration, Aghanim, N., Akrami, Y., et al. 2020, *A&A*, 641, A6.
 Prescott, M. K. M., Martin, C. L., & Dey, A. 2015, *ApJ*, 799, 62
 Ramos Almeida, C., Piqueras López, J., Villar-Martín, M., et al. 2017, *MNRAS*, 470, 964
 Ramos Almeida, C., Bischetti, M., García-Burillo, S., et al. 2022, *A&A*, 658, A155.
 Rémy-Ruyer, A., Madden, S. C., Galliano, F., et al. 2014, *A&A*, 563, A31
 Rupke, D. S. N., Kewley, L. J., & Barnes, J. E. 2010, *ApJ*, 710, L156.
 Searle, L. 1971, *ApJ*, 168, 327
 Tortora, C., Hunt, L. K., & Ginolfi, M. 2022, *A&A*, 657, A19
 Tremonti, C. A., Heckman, T. M., Kauffmann, G., et al. 2004, *ApJ*, 613, 898
 Tumlinson, J., Peebles, M. S., & Werk, J. K. 2017, *ARA&A*, 55, 389
 van Ojik, R., Roettgering, H. J. A., Carilli, C. L., et al. 1996, *A&A*, 313, 25
 Venturi, G., Treister, E., Finlez, C., et al. 2023, *A&A*, 678, A127
 Villar-Martín, M., Vernet, J., di Serego Alighieri, S., et al. 2003, *MNRAS*, 346, 273
 Villar Martín, M., Emonts, B., Humphrey, A., et al. 2014, *MNRAS*, 440, 3202
 Villar-Martín, M., Cabrera-Lavers, A., Humphrey, A., et al. 2018, *MNRAS*, 474, 2302
 Villar Martín, M., Emonts, B. H. C., Cabrera Lavers, A., et al. 2021, *A&A*, 650, A84
 Wang, W., Wylezalek, D., Vernet, J., et al. 2023, *A&A*, 680, A70
 Wotta, C. B., Lehner, N., Howk, J. C., et al. 2016, *ApJ*, 831, 95
 Wright, E.L. 2006 *PASP*, 118, 1711

Table 1. Photoionisation model predictions

Aperture	E(B-V)	[OIII] λ 4363	[OIII] λ 5007	[NII] λ 5755	[NII] λ 6584	[SII] λ 6725	[SII] $\frac{\lambda 6716}{\lambda 6731}$	12+log(O/H)	log(N/O)	$T_{[OIII]}$ K	$T_{[NII]}$ K	n_e cm ⁻³
1	0.074±0.012	0.144±0.014	6.000±0.215	0.019±0.001	1.437±0.114	1.598±0.047	1.316±0.056	8.68±0.15	-0.86±0.11	16565±875	9508±312	149±79
2	0.155±0.015	0.141±0.012	5.802±0.588	0.017±0.001	1.396±0.044	1.507±0.051	1.396±0.026	8.61±0.13	-0.85±0.11	16739±1196	9236±225	34±36
3	0.054±0.013	0.135±0.015	6.043±0.251	0.020±0.002	1.044±0.042	1.467±0.060	1.349±0.048	8.76±0.11	-1.03±0.09	16058±1071	11185±448	100±63
4	0.034±0.013	0.158±0.012	7.290±0.251	0.018±0.002	1.012±0.048	1.359±0.071	1.382±0.027	8.69±0.08	-1.00±0.08	15801±699	10822±543	51±34
5	0.063±0.018	0.142±0.008	7.199±0.322	0.016±0.002	0.991±0.062	1.196±0.056	1.343±0.033	8.77±0.12	-0.99±0.08	15064±493	10325±565	109±41
6	0.046±0.017	0.143±0.010	6.885±0.319	0.019±0.001	1.086±0.063	1.326±0.078	1.321±0.036	8.69±0.12	-0.98±0.11	15433±641	10656±344	141±52
7	0.101±0.014	0.162±0.009	7.342±0.323	0.019±0.001	1.070±0.067	1.419±0.059	1.341±0.036	8.68±0.09	-1.00±0.08	15938±501	10743±353	114±50
8	0.087±0.021	0.128±0.014	5.665±0.326	0.020±0.001	1.291±0.112	1.589±0.088	1.369±0.046	8.76±0.15	-0.93±0.11	16181±1037	10134±391	74±60
9	0.031±0.013	0.145±0.006	6.900±0.316	0.020±0.002	1.195±0.069	1.423±0.072	1.394±0.021	8.72±0.10	-0.94±0.10	15453±442	10495±516	40±33
10	0.105±0.016	0.115±0.019	4.557±0.208	0.020±0.002	1.169±0.079	1.632±0.074	1.411±0.016	8.56±0.20	-0.98±0.11	16888±1484	10580±530	≈35
Nucleus	0.186±0.033	0.086±0.014	6.550±0.310	0.021±0.003	1.497±0.157	0.920±0.059	1.242±0.138	8.66±0.11	-0.56±0.08	12772±785	9825±658	301±270
11	0.000±0.046	0.146±0.021	5.941±0.387	N/A	1.271±0.183	1.455±0.082	1.335±0.017	8.53±0.17	-0.85±0.15	16899±1339	N/A	115±22
12	0.132±0.015	0.113±0.014	3.570±0.170	N/A	1.350±0.061	1.865±0.085	1.450±0.050	8.52±0.14	-0.87±0.11	19540±1235	N/A	16±34
13	0.000±0.038	0.083±0.023	3.197±0.325	N/A	1.378±0.166	1.973±0.228	1.417±0.054	8.71±0.24	-0.89±0.14	17766±2661	N/A	34±47
14	0.031±0.025	0.175±0.035	6.901±0.531	N/A	1.244±0.104	1.684±0.126	1.330±0.029	8.53±0.15	-0.94±0.11	17197±2124	N/A	129±42
15	0.077±0.041	0.198±0.024	7.222±0.808	N/A	0.914±0.115	1.480±0.183	1.316±0.025	8.40±0.12	-0.94±0.13	17989±1652	N/A	145±34
16	0.023±0.015	0.271±0.040	8.844±0.387	N/A	0.647±0.072	1.382±0.319	N/A	8.37±0.08	-1.00±0.11	18829±1648	N/A	N/A
17	0.029±0.020	0.222±0.017	8.941±0.404	N/A	1.123±0.102	1.339±0.146	1.429±0.061	8.49±0.05	-0.87±0.12	16910±754	N/A	33±48
18	0.121±0.012	0.102±0.023	3.917±0.210	N/A	1.097±0.058	1.602±0.191	1.466±0.030	8.56±0.24	-0.93±0.13	17299±2055	N/A	≈75
19	0.027±0.044	0.090±0.028	2.626±0.481	N/A	1.245±0.283	1.125±0.378	1.386±0.039	8.39±0.30	-0.86±0.28	18925±3439	N/A	48±45
20	0.077±0.031	0.087±0.016	3.075±0.420	N/A	1.494±0.282	1.888±0.284	1.396±0.039	8.60±0.25	-0.84±0.20	18398±2835	N/A	41±45
21	0.126±0.059	0.201±0.033	8.234±1.289	N/A	0.716±0.126	0.947±0.164	1.372±0.028	8.44±0.13	-0.94±0.16	16972±1929	N/A	70±38
22	0.000±0.007	0.154±0.012	7.099±0.143	N/A	0.776±0.038	1.164±0.338	N/A	8.44±0.18	-0.97±0.17	15798±608	N/A	N/A

Notes. Model predictions of the O/H and N/O relative abundances, the electron temperatures, $T_{[OIII]}$ and $T_{[NII]}$ and electron densities n_e inferred from the $[\text{SII}]_{\lambda 6731}^{\lambda 6716}$ ratio. The observed, extinction corrected line fluxes used in the models are quoted relative to H β . E(B-V) values were inferred from H α /H β . The spatial location of the apertures can be seen in Fig. 3. Apertures 3 to 9 cover the edge of the ionised bubble. The top (lower) part of the table comprises the apertures in which [NII] λ 5755 is detected (undetected). N/A in the $[\text{SII}]_{\lambda 6731}^{\lambda 6716}$ column means that the doublet ratio could not be measured accurately due to residual sky artefacts. The solar abundances are 12+log(O/H)=8.69±0.04 and log(N/O)=-0.86±0.07 for the Sun (Asplund et al. 2021).